Numerical Study on the Characteristics of Abyssal *T*-Wave Envelopes Controlled by Earthquake Source Parameters

Sukyoung Yun[1], Won Sang Lee*[1], Robert P. Dziak[2], and Haruyoshi Matsumoto[3,4]

Abstract

Hydroacoustics has been successfully applied to detect and locate small-to-intermediate submarine tectonic activities infrequently recorded in land-based seismic arrays. However, to extend the utilization of *T* waves to extract other important earthquake source parameters, such as source strength, the roles of earthquake focal mechanisms, and source depths in *T*-wave envelopes must be thoroughly understood. We performed 3D numerical modeling considering anisotropic source radiation and realistic scattering in the oceanic crust for two focal mechanisms (normal and strike-slip faults) and three depths (5, 10, and 15 km) to investigate the effect of source radiation and focal depth on abyssal *T* waves. By analyzing the synthetic *T*-wave envelopes, we showed that stronger *SV*-energy radiation from a normal-fault earthquake event generates higher-intensity *T* waves of the same source magnitude. The anisotropic source radiation of a double-couple source causes azimuthal changes in the shapes of *T* waves, and deeper earthquakes cause gentle-sloped envelopes; however, the slopes also vary with respect to the azimuths of receivers and focal mechanisms. Temporal changes in the slopes of *T*-wave envelopes of magmatic swarm events near Wordie Volcano, Bransfield Strait, Antarctic Peninsula, imply that the depth dependency can be utilized to determine relative depths for hydrothermal-vent events or sequenced earthquakes.

Cite this article as Yun, S., W. S. Lee, R. P. Dziak, and H. Matsumoto (2022). Numerical Study on the Characteristics of Abyssal *T*-Wave Envelopes Controlled by Earthquake Source Parameters, *Seismol. Res. Lett.* **93**, 2189–2200, doi: 10.1785/0220210264.

Supplemental Material

Introduction

Oceanic *T* waves are seismically generated acoustic waves trapped and propagating within the sound fixing and ranging (SOFAR) channel (Tolstoy and Ewing, 1950), allowing the detection of remote events and determining their locations with better accuracy (Pan and Dziewonski, 2005). Taking advantage of the propagation efficiency, well-defined acoustic sound speed profiles, and slow propagation speed (~1.47 km s^{-1}) in the water column, scientists have successfully applied hydroacoustics to identify tectonic activities of the underlying seafloor that are barely recorded by land-based seismograph networks (Dziak *et al.*, 1995; Dziak and Fox, 1999; Fox *et al.*, 2001; Bohnenstiehl *et al.*, 2003). Such detailed information on the spatial and temporal distribution of submarine tectonic activities has considerably improved our understanding of oceanic-tectonic processes.

Extensive efforts have been made to improve the constraints on seismic source parameters (e.g., location of epicenter and earthquake magnitude) by employing hydroacoustic observations in the global ocean. In particular, one of the important source parameters in seismology is earthquake magnitude, which can be estimated by empirical relationships at the places of interest compared to the acoustic source level (Dziak *et al.*, 1997; Dziak, 2001; Fox *et al.*, 2001) or the energy flux of *T* waves (Okal *et al.*, 2003; Bohnenstiehl *et al.*, 2013). Source depth is another fundamental parameter that characterizes the source of events and the type of earthquake sequence that occurs in the oceanic crust and midocean ridges. However, hydrophones can detect only converted acoustic waves propagated through water, which inhibits the accurate determination of the source depth. Ocean-bottom seismographs provide more detailed information about oceanic events when installed nearby (Tolstoy *et al.*, 2006).

Determination of seismic source parameters from converted acoustic waves requires understanding on the physical processes of *T*-wave generation. Downslope conversion and multiple reflections of converted acoustic waves between the sea surface and sloping seafloor (Tolstoy and Ewing, 1950; Johnson *et al.*, 1963; Talandier and Okal, 1998) successfully accounted for

1. Division of Glacial Environment Research, Korea Polar Research Institute, Yeonsu-gu, Incheon, Republic of Korea, https://orcid.org/0000-0003-0778-7259 (SY); https://orcid.org/0000-0002-1074-7672 (WSL); 2. Pacific Marine Environmental Laboratory, National Oceanic and Atmospheric Administration, Newport, Oregon, U.S.A.; 3. Oregon State University/Cooperative Institute for Marine Resources Studies, Hatfield Marine Science Center, Newport, Oregon, U.S.A.; 4. NOAA/Pacific Marine Environmental Laboratory, Newport, Oregon, U.S.A.

*Corresponding author: wonsang@kopri.re.kr

the generation of horizontally propagating T waves in regions near islands or continental shelves. For the cases of T-waves excitation in gently sloping or almost flat bathymetry regions far below the SOFAR channel, scattering at rough bathymetry above the source location was proposed as the key mechanism of the "abyssal" T-wave excitation by several studies (Walker *et al.*, 1992; de Groot-Hedlin and Orcutt, 1999, 2001; Park *et al.*, 2001). The abyssal T waves are characterized by higher dominant frequency and weaker amplitude than the T waves generated in shallower islands. de Groot-Hedlin and Orcutt (1999, 2001) synthesized T-wave envelopes using a numerical 3D model that corresponded well with observations. Their assumptions are: (1) the T waves are excited by small-scale scatterers at a rough seafloor, (2) acoustic modal amplitude is proportional to the product of the converted P-wave amplitude and the relative displacement of the normal modes on the seafloor. Their studies showed that T-waves excitation mainly depends on a seafloor depth and P-wave energy on the seafloor. However, the realistic spatial distribution of P-wave energy on the seafloor could not be simulated according to their model because they considered an isotropic point source and ignored scattering attenuation in the oceanic crust. Park *et al.* (2001) accounted for the abyssal T-wave generation by adopting the modal scattering theory in 2D, which highlights that fault mechanisms are responsible for the efficiency of T-wave excitation. Balanche *et al.* (2009) developed a numerical 2D model that could handle the conversion of seismic–acoustic waves at the crust–water interface and implement a double-couple earthquake source. Furthermore, they confirmed that S waves are more efficient than P waves in producing energetic T waves, which was originally proposed by Park *et al.* (2001). A study by Jamet *et al.* (2013), using a 2D spectral element method, successfully reproduced two distinct energy peaks at T-wave arrivals typically observed in real T waves generated from double-couple earthquake sources (normal and strike-slip faults). They argued that hydroacoustics could potentially provide information about the earthquake source parameters.

Although these numerical studies enrich our knowledge of the generation and propagation of T waves, only a few attempts have been made to emphasize the effect of source depth (Schreiner *et al.*, 1995; Yang and Forsyth, 2003) that primarily control both the appearance of T-wave arrivals (T-wave packet rise time) and acoustic source level.

In this study, we systematically examined the effect of earthquake source radiation and focal depth on abyssal T-wave envelopes by developing a numerical model designed to deal with both elastic-wave energy propagation in the heterogeneous oceanic crust and long-range acoustic wave propagation in a water column. Our numerical modeling verified that the shapes of T-wave envelopes vary with the back azimuth of the receiver by anisotropic source radiation, and the source depth changes the slope of the T-wave envelopes. Because a combination of fault types, depths, and back azimuths affects T-wave envelopes, it remains challenging to extract individual source parameter information explicitly from T waves. However, we showed that hydroacoustics can be utilized to investigate the vertical migration pattern of seismic sources as their focal depth changes in the ocean crust, yet their source parameters are similar, as exhibited by a gradual slope of the T-wave envelopes from volcanic tremors recorded in the Bransfield Strait, Antarctic Peninsula.

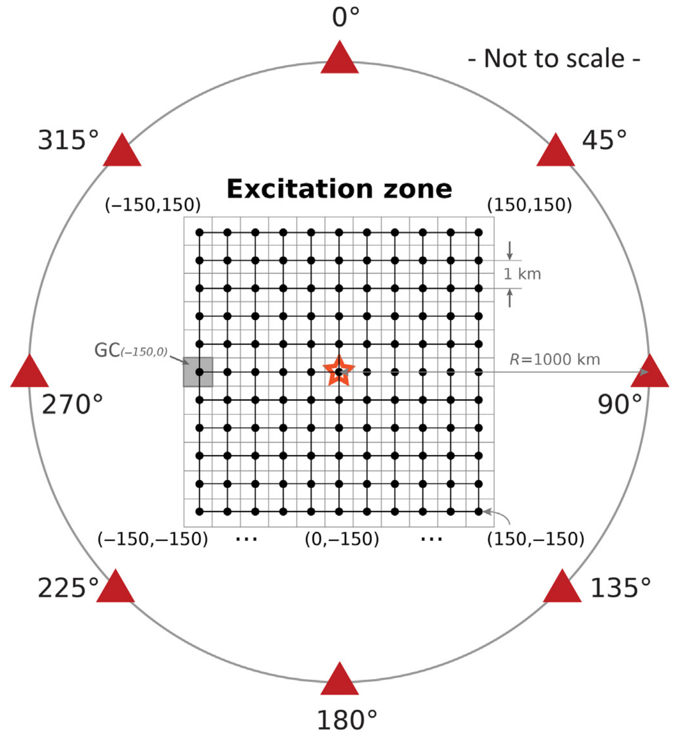

Figure 1. Schematic of the T-wave excitation zone and receiver array configuration (map view) used for numerical simulations in this study. Eight virtual acoustic stations are deployed along a circle of 1000 km in radius (R) at 600 m underwater. A 300 × 300 rectangular grid with 1 km spacing is established for the excitation zone. Point shear sources (double couple) are placed in the center of the array with three depths (5, 10, and 15 km) below seafloor. When a seismic energy particle arrives at a point within a certain grid cell (GC(i,j)) at a given time, E(i;j;t) represents seismic energies for the cell at t. The accumulated energy in time is converted to acoustic pressure and builds up T wave.

Materials and Methods

Model description

To examine the effects of seismic source parameters on the characteristics of abyssal T-wave envelopes, we designed numerical experiments for the combinations of two fault types (normal and strike-slip) and three source depths (5, 10, and 15 km). Figure 1 illustrates a modeling scheme, and the parameters used for the modeling are listed in Table 1. To compute seismic P- and SV-wave energy at receiver cells at the seafloor at a given period, we employed the slightly modified the direct simulation Monte Carlo (DSMC) method (Yoshimoto, 2000). The computed

TABLE 1
Parameters Used for Numerical Simulation

Source Parameters						
Fault type	Normal (strike $\varphi = 0°$, dip $\delta = 45°$, and rake $\lambda = -90°$)					
	Strike-slip ($\varphi = 0°$, $\delta = 90°$, and $\lambda = 180°$)					
Focal depth (km; below the seafloor)	5, 10, and 15					
Radiated energy and particle numbers	Normal-fault event			Strike-slip-fault event		
	Radiated energy to total energy	Number of particles	Energy per particle	Radiated energy to total energy	Number of particles	Energy per particle
P wave	4%	5.0×10^5	4	4%	2.0×10^6	1
SV wave	76%	9.5×10^6		16%	8.0×10^6	
Excitation Zone Configuration on Seafloor						
Dimension (km)	300 × 300					
Cell size (km)	1 × 1					
Receiver Array Configuration						
Number of stations	8					
Azimuthal spacing (°)	45					
Epicentral distance (km)	1000					
DSMC Input Parameters						
Number of particles	107					
Δt (s)	0.02					
Total duration (s)	100					
$\Delta\theta, \Delta\varphi$ (°)	1.8					
Scattering coefficient (g_0; km^{-1})	0.11 (layer 1) and 0.01 (layer 2)					
***T*-Wave Propagation**						
T-wave velocity (km s^{-1})	1.477					
T-wave attenuation	Geometrical spreading (r^{-1}), no intrinsic absorption applied					

DSMC, direct simulation Monte Carlo.

incident seismic energies were translated into acoustic pressure, and the value was set at the center of each grid cell. Subsequently, we treated each point as a secondary source to excite acoustic waves proportional to the acoustic pressure (de Groot-Hedlin and Orcutt, 1999). Further detailed descriptions of the DSMC, seismic-to-acoustic energy conversion, and *T*-wave generation are provided in the DSMC Modeling and Energy Conversion at Seafloor and T-wave Envelope Generation sections.

We assumed a zero-gradient seafloor, that is, a flat seabed, for simplicity in conducting the numerical model. Although rough bathymetry may contribute to the excitation of *T* waves to some extent (de Groot-Hedlin and Orcutt, 1999, 2001; Park *et al.*, 2001), it does not notably affect the shape of the *T*-wave envelopes, in which we investigated the spatial distribution of acoustic wave energy and source depth migration for a flat seabed with small-scale uniform roughness.

Receiver array and source parameters

We configured a receiver array with eight virtual acoustic stations deployed every 45° along a circle with a radius of 1000 km (Fig. 1). Double-couple earthquake sources were placed at the center of the array at depths of 5, 10, and 15 km below the seafloor. We calculated the radiated seismic-wave energy for two simple fault geometries, normal (strike $\varphi = 0°$, dip $\delta = 45°$, and rake $\lambda = -90°$) and strike-slip faults ($\varphi = 0°$, $\delta = 90°$, and $\lambda = 180°$), to derive the energy ratios between the *P*, *SV*, and *SH* waves (E^P, E^{SV}, and E^{SH}). In this study, we considered only the energy contribution of *P* and *SV* waves because *SH* waves (horizontally polarized, no vertical particle motion) cannot be converted into acoustic waves at the solid–water interface (Shearer, 1999). For a pure point shear source in a Poisson solid, the expected E^S/E^P ratio of 23.2 (Venkataraman and Kanamori, 2004) is independent of the focal mechanism. The ratio of the radiated energy of *SV* and *SH* components can be calculated corresponding to the different focal mechanisms following the methodology outlined by Boore and Boatwright (1984), which provides the energy portions of *SV* waves relative to the total radiated energy as approximately 76% and 16% for the normal- and strike-slip-fault event sources used in this study, respectively. We selected the focal depths for modeling (5, 10, and 15 km) by referring to a study by Abercrombie and Ekström (2001), who carefully constrained source locations, and found that seismic slip (brittle failure) occurs in the oceanic crust from near surface to ~20 km depth.

DSMC modeling and energy conversion at seafloor

We adopted the DSMC method (Yoshimoto, 2000), which has been widely applied to simulate seismic-wave energy propagation in 3D heterogeneous earth media (e.g., Lee *et al.*, 2003, 2006), such as oceanic crust. We slightly modified the method to address a shear (double-couple) source problem and calculated the incident seismic-wave energy later translated into acoustic pressure on the seafloor at a given time. The modified DSMC technique can handle: (1) anisotropic radiation of *P* and *SV* waves from pure double-couple sources, (2) multiple isotropic scattering, (3) intrinsic attenuation, and (4) 3D propagation in layered earth velocity structures.

We first numerically calculated *P*- and *SV*-energy radiation patterns as a function of θ and ϕ in the spherical polar coordinate system (Aki and Richards, 2002) for the two different types of faults (Table 1). Integrating radiated energy within 1.8° spacing for both θ and ϕ, we generated 4000 pairs over the entire solid angle.

The radiation patterns serve as a probability density function to determine the number of energy particles projected from the source for each (θ, ϕ) pair. In other words, as we project a certain number of energy particles (10^7 in total for this numerical experiment), the particles are distributed in proportion to the amplitude of the calculated *P*- and *SV*-radiation patterns. Because the sum of the radiated *P* and *SV* energies of the normal-fault event is four times larger than that of the strike-slip fault, the unit energy per particle for the normal-fault case is set as four times the unit energy of the strike-slip fault simulation. The number of energy particles for the *P* and *SV* waves and their energy per particle corresponding to each fault type (normal and strike slip) are listed in Table 1. The energy particle represents a seismic wavelet of unit energy (Yoshimoto, 2000). When an energy particle travels through the heterogeneous earth medium, the particle propagates following ray theory until it meets a scatterer. The mean free path of the scattering medium is defined by the total scattering coefficient (g_0). Further details can be found in Yoshimoto (2000).

The physical properties of different media used here are adopted from studies on midocean ridges and strike-slip fault

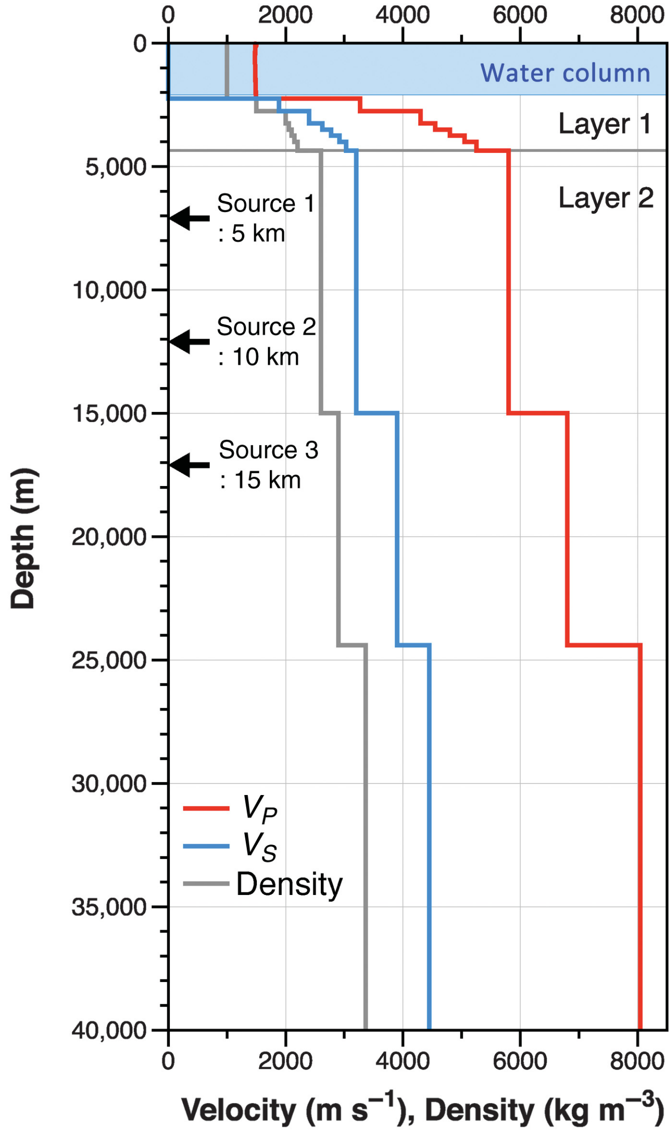

Figure 2. *P*- (red line) and *S*-wave (blue line) velocity and density (gray line) profiles in different media (water column, ocean-bottom sediments, oceanic crust, and upper mantle). We used a two-layered attenuation model that has different scattering coefficients in the earth medium. The location of double-couple sources (5, 10, and 15 km below the seafloor) are marked by black arrows.

systems where abyssal *T* waves are generated (Park *et al.*, 2001). Figure 2 shows the velocity and density profiles of the water column, ocean-bottom sediments, oceanic crust, and upper mantle in the northeast Pacific Ocean. We considered a two-layer attenuation model and assumed that point-like isotropic scatterers are randomly distributed in the solid-earth medium. The total scattering coefficients g_0 in the oceanic crust were 0.11 km^{-1} and 0.01 km^{-1} for layer 1 (0–2.1 km) and layer 2 (deeper than 2.1 km), respectively, which correspond to the results of an in situ seismic attenuation study in the East Pacific Rise (layer 1; Swift *et al.*, 1998) and the average value in the crust (layer 2; Sato and Fehler 1998). Intrinsic Q-values of 1000 (Hoshiba, 1997) and 2000 (Gusev, 1995) were provided for layers 1 and 2, respectively. The model parameters used in the DSMC simulations are listed in Table 1.

We created a grid of 300 × 300 1 km cells representing the seafloor in the x and y direction to establish a sufficiently wide excitation zone, so that most of the seismic energy arriving from the deepest source (15 km) could be captured (Fig. 1). Each seismic energy packet experiences attenuation constrained by an intrinsic Q-value while it travels through the heterogeneous medium. When an energy particle arrives at a certain grid cell, the attenuation is applied to the energy particle at a given lapse time, and a seismogram envelope is built on the grid cell. Then, the energy particle that hits the solid-earth-water boundary (seafloor) propagates either into the water column (converted acoustic pressure waves) or back to the earth medium (reflected waves). The energy ratio of the seismic waves reflected and refracted at the seafloor was calculated by following the method developed by Ergin (1952). The converted acoustic wave particles play a secondary source role in the T-wave excitation.

T-wave envelope generation

We followed the T-wave excitation modeling technique developed by de Groot-Hedlin and Orcutt (1999) assuming that the T-wave excitation is proportional to the acoustic pressure on the seafloor. The acoustic pressure (p) is directly proportional to the square root of acoustic intensity, which is calculated from incident seismic wave energy.

To explore the azimuthal pattern of T waves generated from double-couple earthquake sources (normal and strike-slip faults), we placed eight virtual receivers with a 45° spacing along a circle with a 1000 km radius and sources at the center of the receiver array (Fig. 1). Given the epicentral distance of 1000 km and the wavelength of 0.3 km for T waves at 5 Hz, we can treat each cell as a point-like source for T-wave excitation assuming the far-field approximation because a unit grid cell (1 × 1 km) is only 6% of the upper bound $(1000 \times 0.3)^{1/2} = 17.32$ km. Travel time from each grid cell (a secondary source for T-wave excitation) to the surrounding receivers can be calculated by assuming a constant T-wave velocity of 1.47 km/s in the water column. We did not consider modal dispersion in T-wave propagation following de Groot-Hedlin and Orcutt (2001) and Park *et al.* (2001). During their propagation, the acoustic waves excited from the seafloor (at each grid cell) lose energy through 2D geometrical spreading effects; however, energy loss due to absorption of acoustic energy in seawater is negligible below 100 Hz (Brekhovskikh and Lysanov, 2003). In addition, we assumed that the sound speed profile did not vary along the propagation path. Consequently, we could synthesize T-wave envelopes by integrating wave energies arrived at each receiver within a 2 s time window (0–2, 2–4, 4–6 s, …).

Results

DSMC results and *T*-wave directivity

The spatial distributions (surface map view) of normalized seismic energy transmitted into the water column on the seafloor and their corresponding synthetic T-wave envelopes at each receiver are shown in Figure 3a (the normal fault at 5 km in depth) and Figure 3b (the strike-slip fault at 5 km in depth). The energy distributions are constructed by the summation of acoustic energy on each grid through all timesteps (100 s after the origin time), and then, they are normalized by the largest amplitude of seismic energy over all source combinations, which is obtained from the maximum energy peak for the normal-fault event with a source depth of 5 km. The sound pressure levels of the T-wave envelopes were normalized as the highest amplitude value among the entire envelopes to become 0 dB (root power quantity).

The seafloor energy distribution shows different radiation patterns depending on the fault type. For the normal-fault case, energies are concentrated at two points, 4 km away from the epicenter in the north–south direction. For the strike-slip-fault case, there are four energy highs in four orthogonal directions, 4.2 km away from the epicenter. These multiple energy highs on the seafloor are induced by the nonisotropic elastic energy radiation of double-couple sources, and they ultimately cause directional changes in the shapes of T-wave envelopes and their maximum amplitudes. When acoustic waves from several energy highs arrive simultaneously at a receiver, a strong unique peak is formed in the envelope owing to the overlap. In contrast, dispersed acoustic wave arrivals from the energy highs result in T-wave envelopes with weaker and multiple peaks. As we assume that the T-wave velocity is constant along the propagation path, the azimuthal variation of the T-wave envelopes can be attributed to only the difference in distance between receivers and energy-concentrated spots. These features can be observed in Figure 3a,b; the levels of the maximum peak are higher than others when the envelopes have unique peaks (envelopes at 90° and 270° stations for the normal-fault events and envelopes at 45°, 135°, 225°, and 315° for the strike-slip-fault event).

Multiple scattering redistributes seismic energy without energy loss, which creates the asymmetric shapes of synthetic T-wave envelopes. Given the nature of the process, it does not much contribute to perturbing arrival times of T waves in the shallow oceanic crust. Rather, it generates longer coda waves as the energy particles stay longer in the earth medium.

The peak amplitudes and their arrival times with respect to the station azimuth for all source combinations are shown in Figure 4. The red and blue open dots represent the normal- and strike-slip-fault events, respectively. The peak amplitude at each station has directivity, and the fault type differences are more significant than the directional differences. The peak amplitude of the normal-fault event is generally 5 dB higher than that of the strike-slip-fault event, corresponding to a

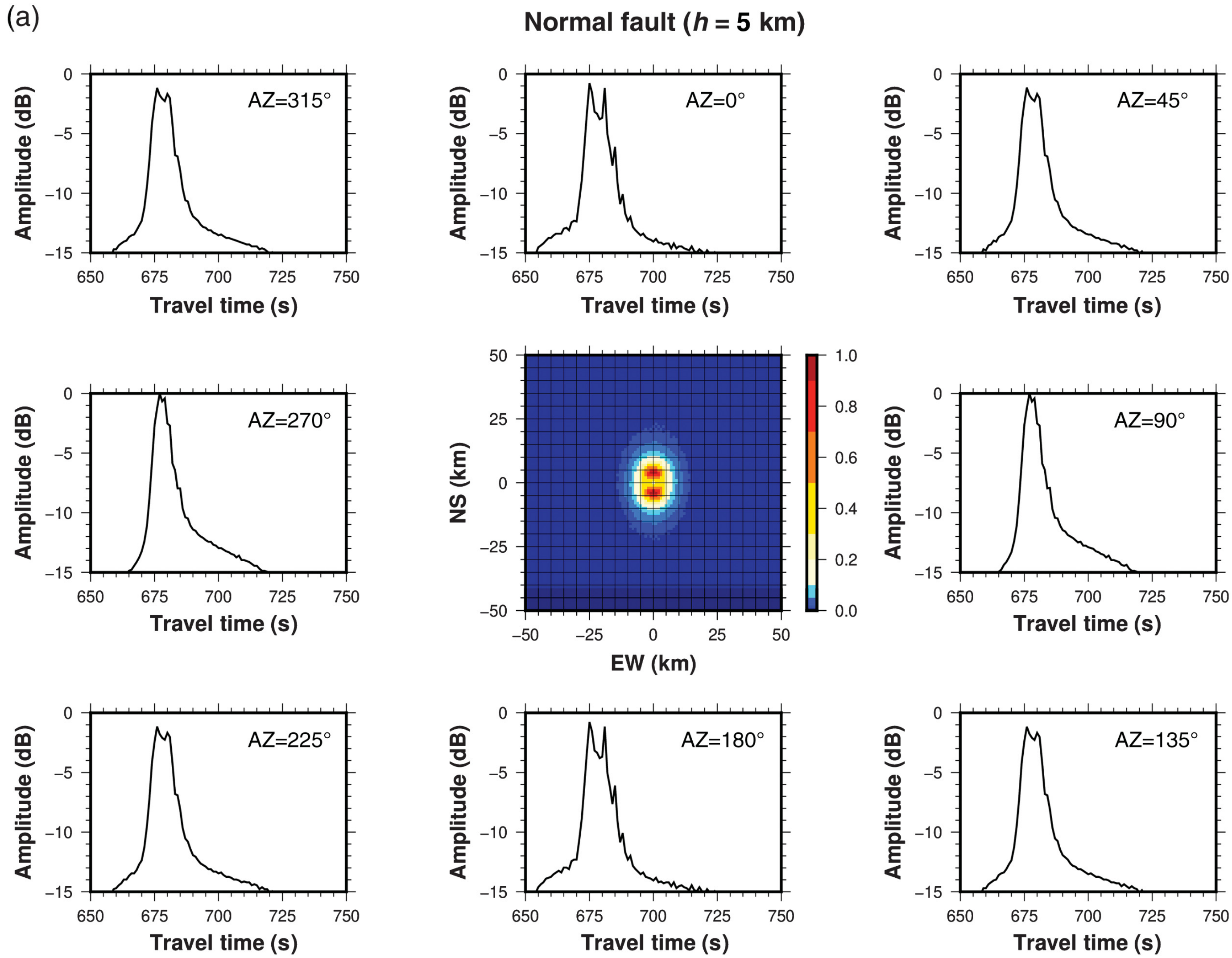

Figure 3. (a) Normalized seismic energy distribution plot for the normal-fault event at 5 km in focal depth over a 100 ×100 km grid on the seafloor. Plots for synthetic *T*-wave envelopes at eight acoustic receivers are situated around. The energy distribution (in the middle) is constructed by the summation of acoustic energies at each grid through entire duration (100 s after origin time). Typically, surface energies are concentrated at two spots, ~4 km away from the epicenter in the north–south direction. The anisotropic energy distribution on the seafloor builds the directional variation on the *T*-wave envelopes. Seismic energy at the seafloor and simulated *T*-wave envelopes are normalized by the maximum values of the normal-fault event for comparison. (b) Case for the strike-slip-fault event. Note that the energy level is weaker than the normal fault, which is attributed to smaller *SV* energies radiated from the strike-slip-fault event. Seismic energy at the seafloor is concentrated on four orthogonal directions. (*Continued*)

5 dB sound level difference and approximately 1.8 times stronger pressure. These significant differences in the equivalent seismic magnitude are due to the stronger *SV*-energy radiation of normal-fault events.

Figure 4b shows the polar diagrams of the arrival times of the peak point in the envelope to the station azimuth. The various arrival times indicate that the strongest waves do not always originate from the epicenter, the center of the circular array. The discordance between energy highs on the seafloor and epicenter causes variations in the peak arrival times. The multiple peaks due to the anisotropic source radiation make it difficult to locate the exact epicenter using the traditional method of picking peak points of *T* waves. Yang and Forsyth (2003) suggested that location errors can be reduced by selecting the crossing point of two lines fit to the rising and decaying parts of the envelopes. This technique has the advantage of locating the epicenters instead of the maximum energy radiators. Thus, quantitative assessment of location errors considering multiple peaks created from the synthesized *T*-wave envelopes should be considered in future hydroacoustic location analyses.

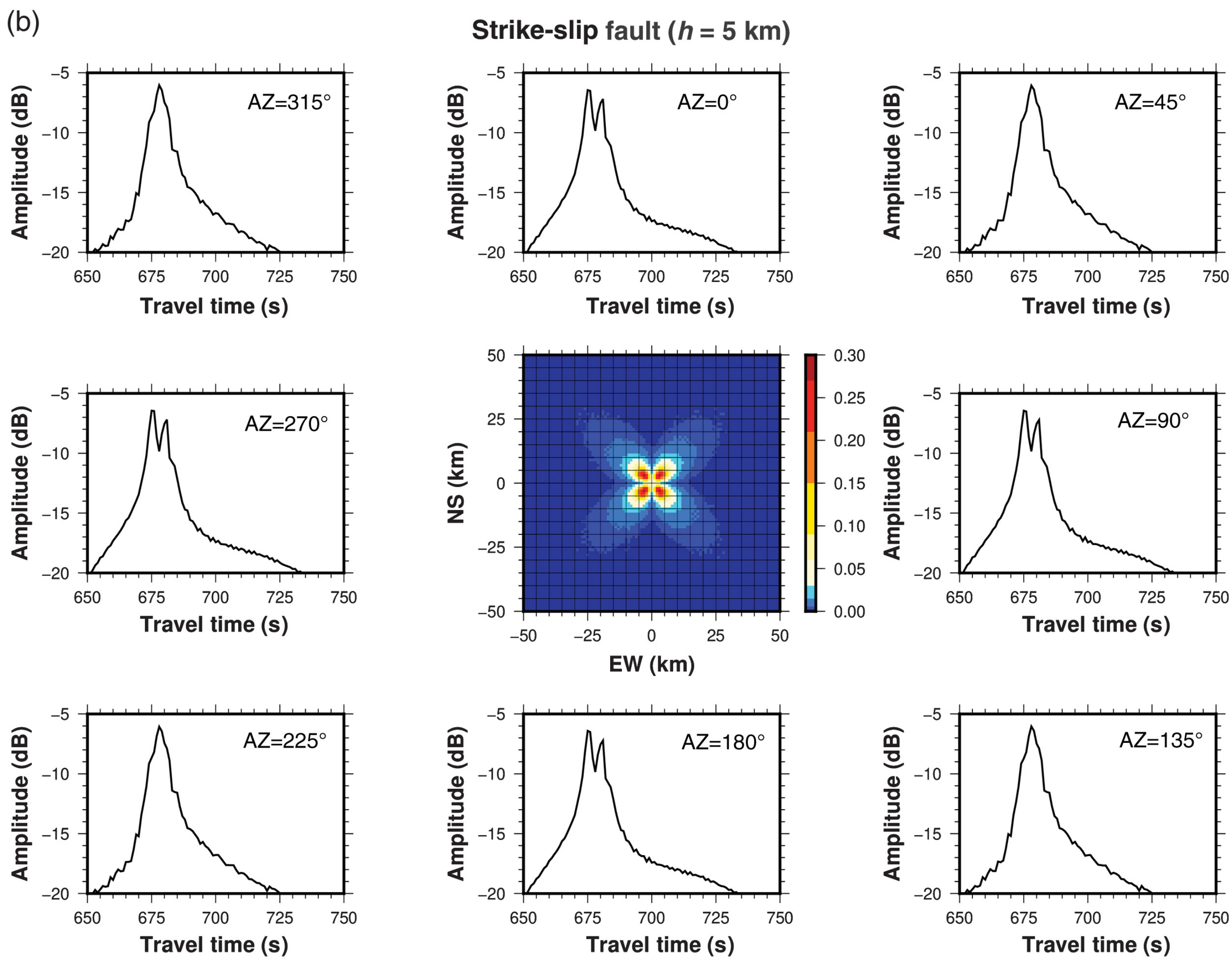

Figure 3. Continued

Depth-dependent characteristics

Schreiner *et al.* (1995) reported that the changes in the rise time of a *T*-wave packet are attributed to the changes in source depths. Accordingly, we estimated the rising slopes (ΔAmplitude in dB/Δt) of the synthetic envelopes for the three focal depths of 5 km, 10 km, and 15 km to examine the depth-dependent characteristics of *T*-wave envelopes. Figure 5a,d shows the synthetic *T*-wave envelopes for the three focal depths and their best-fitting lines on the rising part of the envelopes. The least-squares fit of the envelopes from the normal-fault (Fig. 5a) and strike-slip-fault events (Fig. 5d) are plotted as red and blue lines, respectively. The averaged slopes for the normal-fault (red) and strike-slip-fault events (blue) with respect to the different source depths are plotted in the upper center (Fig. 5b), illustrating that a shallower earthquake generates a steeper envelope with stronger peaks, whereas the deeper earthquake generates a lower inclined envelope with weaker peaks.

Figures S1 and S2 are the same plots as Figure 3 but for 10 km and 15 km in focal depth. The seismic energy distribution maps show that the stronger energy concentrates near the epicenter for a shallower event whereas it becomes dispersed more evenly in wider area for deeper events. The longer duration and the gently emerging onset of the *T*-wave envelopes are attributable to the broadly dispersed energy distribution on the seafloor for deeper events shown in Figure 5.

Figure 5c shows the estimated slopes for various sources with respect to the azimuth. This diagram shows that the slopes vary not only with the source depth but also relative to the focal mechanism and azimuth, which is an obstacle to constraining the source depth using *T* waves. However, the fact that the slopes of the deeper source are always smaller than the slopes

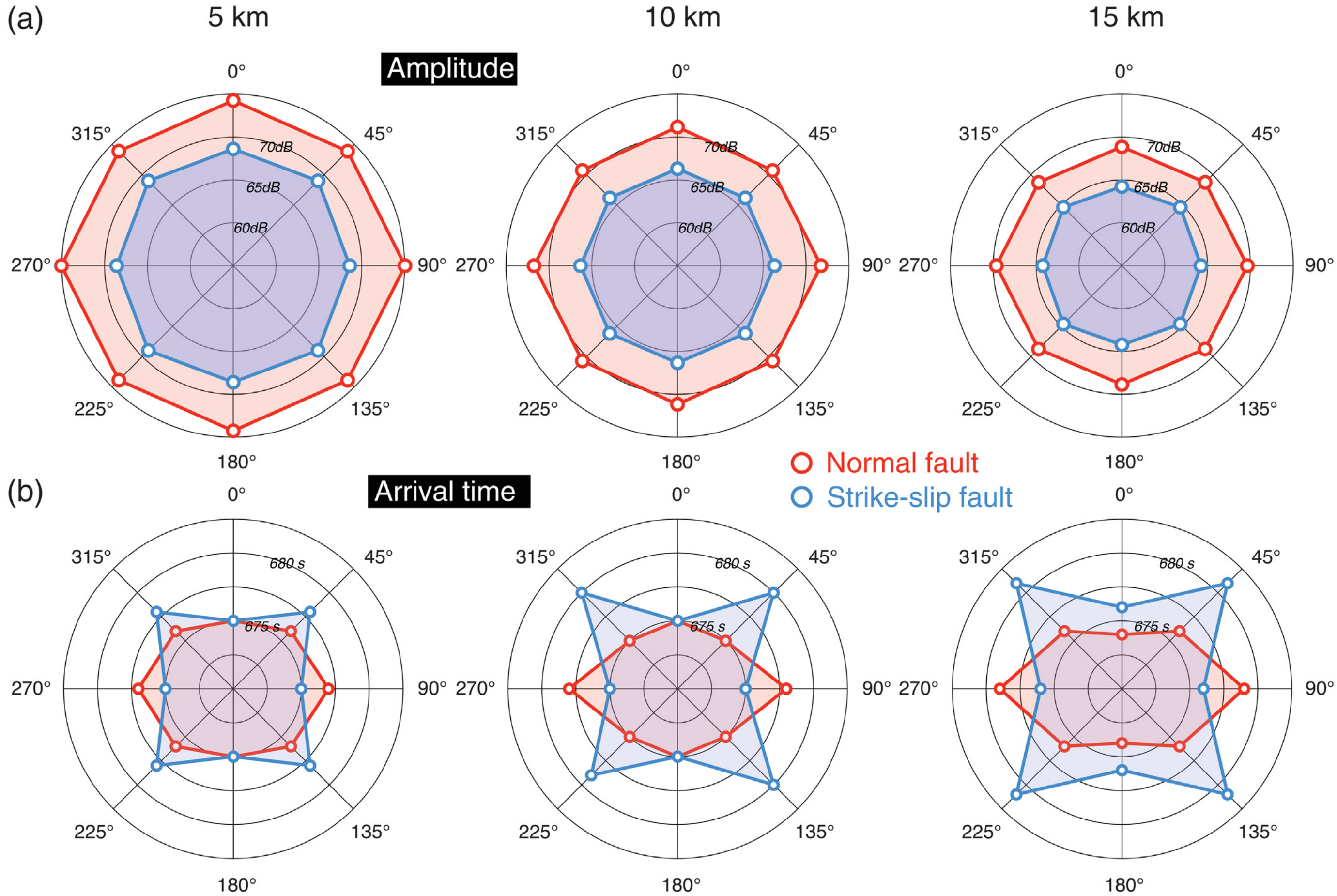

of the shallower source for the same focal mechanism implies that the T waves can be utilized to investigate the vertical migration pattern of seismic sources when source parameters other than focal depth are the same.

Figure 4. (a) Polar diagrams of peak amplitudes regarding station azimuth for the normal-fault (red) and the strike-slip-fault events (blue). For all three depths, peak amplitudes of normal-fault events are higher than those of strike-slip-fault events. It is theoretically valid as normal-fault events radiate more *SV* energy converted into acoustic *T* waves. Peak amplitudes for both fault types become smaller than source depth gets deeper. (b) Plots represent arrival times of peaks in amplitude regarding station azimuth. Early arrivals are plotted closer to the center. The discordance between the locations of energy highs on the seafloor (Fig. 3a,b) and the epicenter results in directional variations in the peak arrival times.

Application of modeling results to *T*-wave observations

We performed least-squares slope fits to the rising part of real T-wave envelopes from tectonomagmatic earthquake swarm events to observe the migration of focal depths. Korea Polar Research Institute National Oceanic and Atmospheric Administration (KOPRI and NOAA) deployed seven hydrophones in the Bransfield Strait in December 2005–2006, and 284 swarm events continued for 2 hr from 03:45 on 26 August near the Wordie Volcano were detected by the hydrophone array (Dziak *et al.*, 2010). Slope fits were applied to the data from one hydrophone, deployed at 62° 14.999′ S, 57° 6.103′ W, following application of a fourth-order Butterworth band-pass filters (4–8 Hz). The slopes of the T-wave envelopes were calculated by least-squares linear regression to the log of the mean square envelopes. The spike-shaped envelopes were well fitted using windows with lengths of 0.2 s, starting from 0.28 s before the peak point of the envelope. Figure S3 presents one of the swarm events occurred at 03:59 (UTC) on 26 August 2006, and a linear fitting (red line) to the rising part of the envelope. The slopes (ΔAmplitude/Δt) of 59 well-fit events are plotted in Figure 6. Figure 6a shows the lateral distribution of the swarm events, in which the origin times of the events are distinguished using colors from yellow to purple. No significant lateral migration pattern was observed; however, the event's T-wave envelope slope versus origin time (Fig. 6b) shows a decrease through time. Because the swarm events occurred closely together in time (2 hr) and space (within 6 km in radius) in the region, the propagation paths to the receiver are very similar to each other. According to the in situ observation and modeling results shown here, decreasing slopes can be caused by vertical migration of the earthquakes to deeper in the ocean crust. The descent of swarms

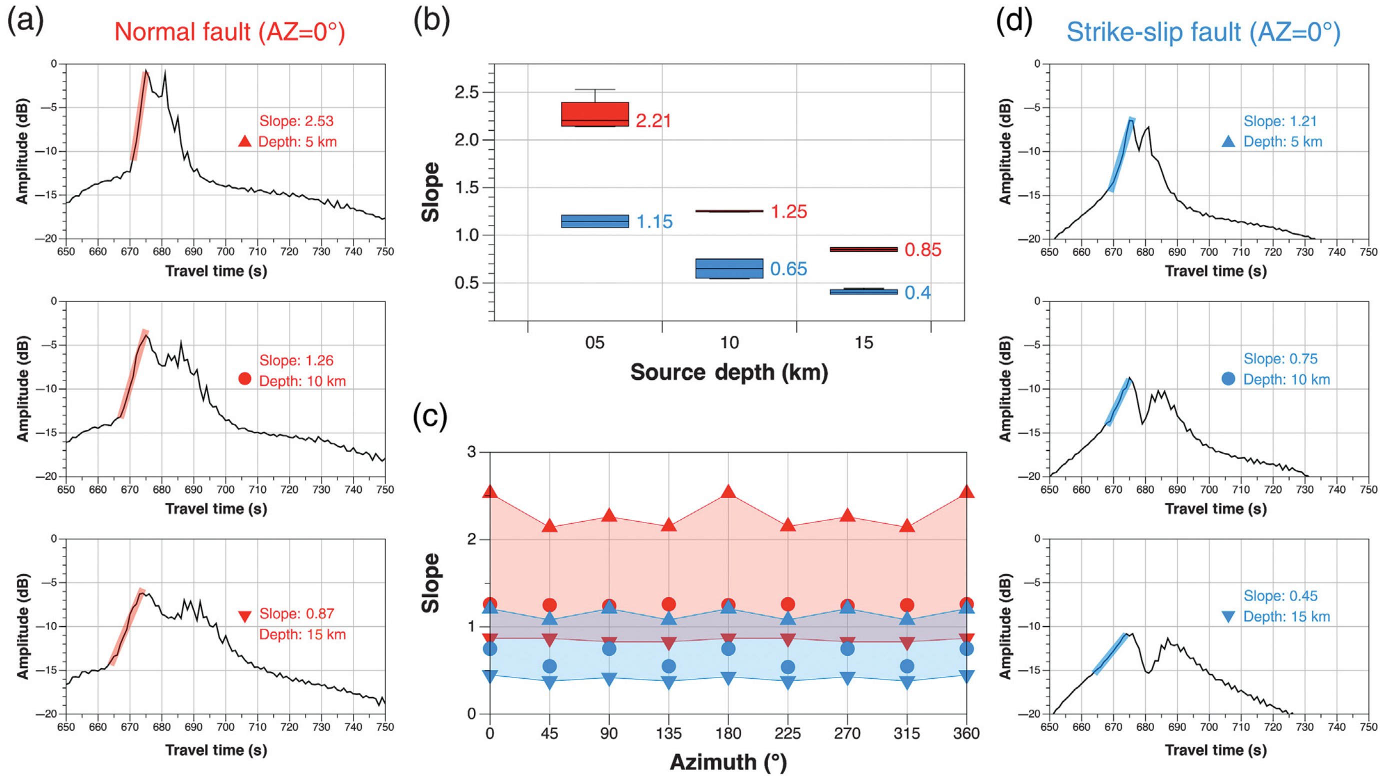

Figure 5. (a) Synthetic *T*-wave envelopes for three focal depths of 5 km, 10 km, and 15 km at a station (0°), and their best-fit lines on the emergence of the envelopes. The least-squares fit on the envelopes for the normal-fault event and the strike-slip-fault events are plotted as red and blue lines (d), respectively. Shallower earthquakes generate steeper envelopes with higher peaks. (b) Averaged slopes for normal-fault (red) and the strike-slip-fault events (blue) regarding source depth. (c) Calculated slopes regarding station azimuth. Slopes vary with both source depth and azimuth. Note that slopes systematically decrease for deeper sources in both fault types. Slopes for the normal-fault case are generally steeper than those for the strike-slip fault at the same source depth.

can be related to magma drainage caused by pressure changes in the conduit (Fukao *et al.*, 1998) or degassing processes in the magma (Kazahaya *et al.*, 1994; Ogiso *et al.*, 2015). Although a more detailed examination of the Wordie Volcano earthquake source characteristics is beyond the scope of this study, we anticipate this will be the focus of future analysis.

Discussion

Efforts to investigate seismic source parameters using *T* waves are underway to understand oceanic-tectonic activities not well recorded by land-based seismic arrays. Other *T*-wave focused researchers have reported empirical relationships between seismic magnitudes and *T*-phase amplitudes (Johnson and Northrop, 1966; Walker *et al.*, 1992), *T*-wave durations (Okal and Talandier, 1986), and acoustic source levels of *T* waves (Dziak *et al.*, 1997; Fox *et al.*, 2001). According to our modeling results, the *T*-wave parameters are not only a function of the source magnitudes but also of the focal mechanism, depth, and azimuth of the receiver. Dziak (2001) showed that the influence of seafloor fault orientation on source levels prevented derivation of a universal scaling law between seismic magnitudes and acoustic source levels. This means that a direct correlation between acoustic source level and seismic magnitude can be obtained only in certain tectonic settings with consistent earthquake source parameters. Moreover, Yang and Forsyth (2003) obtained a good correlation between the maximum amplitudes of the *T*-wave and surface-wave magnitudes by constraining source type, source depth, source region, and path. To overcome the limitation of the acoustic source levels, Okal *et al.* (2003) introduced the *T*-phase energy flux value, which is an integration of the energy recorded in the *T*-wave train. Bohnenstiehl *et al.* (2013) also estimated acoustic energy radiation by calculating the production of the signal power and duration of *T* waves for volcanic events. These approaches attempted to measure the total amount of acoustic energy radiated from an event. Table 2 shows the normalized total acoustic energy transmitted into the water column estimated in the model. The focal depth does not significantly differentiate the total energy, whereas a normal-fault event generates acoustic energy more than double the strike-slip-fault event. Therefore, integrating the acoustic energy on the entire wave train would be the best way to assess source magnitudes using hydroacoustics; however, scaling with the magnitude should be applied separately to the different fault types.

Previous model studies (de Groot-Hedlin and Orcutt, 1999, 2001; Park *et al.*, 2001) indicate that seafloor bathymetry is the leading factor to determine the shape of *T* waves. Furthermore,

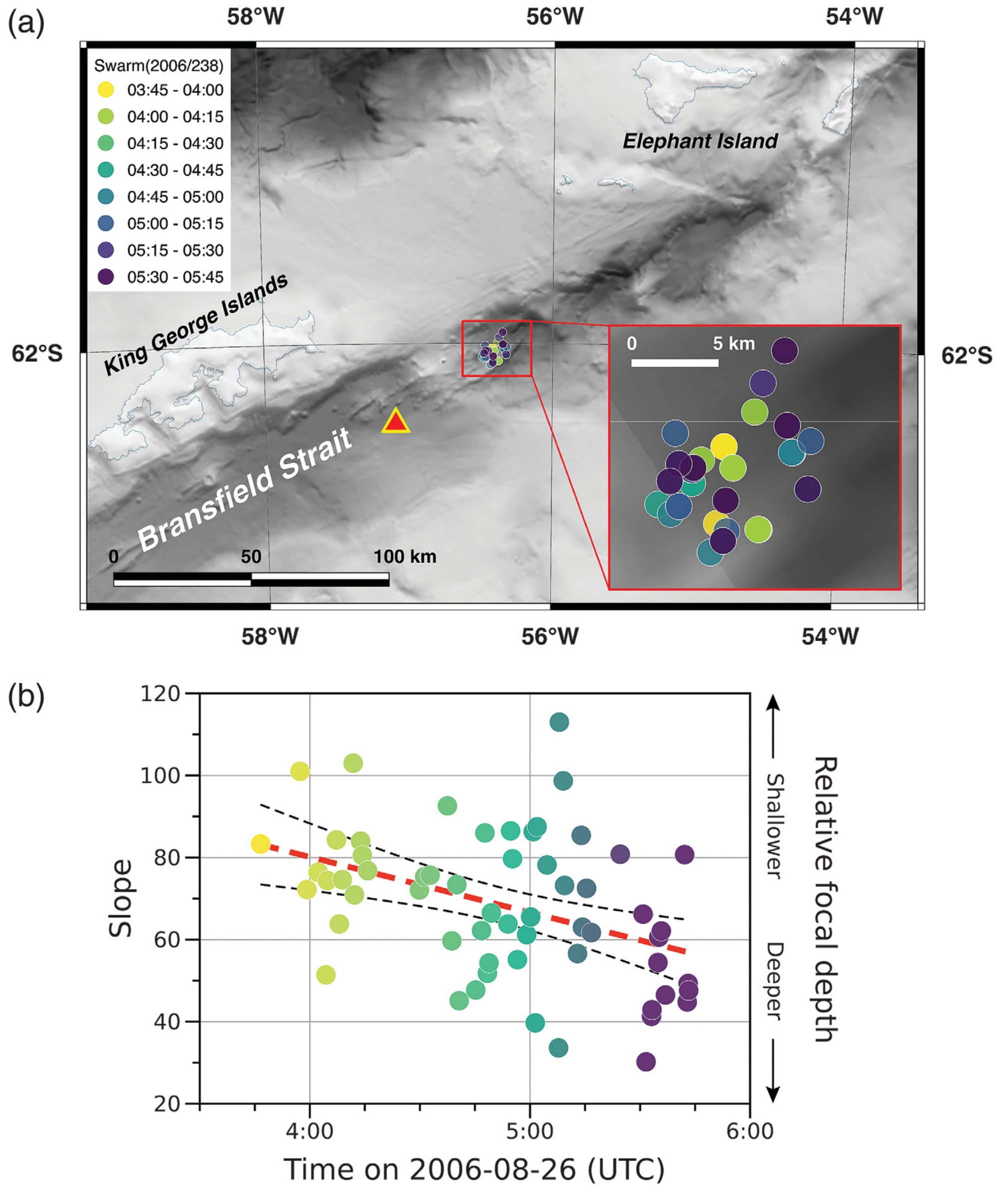

Figure 6. Temporal variations in the onset's slope of *T*-wave envelopes by analyzing volcanic swarms associated with Wordie Volcano, Bransfield Strait, Antarctic Peninsula. In total, 59 events are selected by a visual inspection out of 284 swarm events that occurred during 03:45–05:45 (UTC) on 26 August 2006. The observation data have been collected by the Korea Polar Research Institute National Oceanic and Atmospheric Administration (KOPRI-NOAA) hydrophone array (Dziak *et al.*, 2010). (a) Volcanic swarm events occurred closely together in time (2 hr) and space (within 6 km in radius) in the region. Occurrence time is shown in 15 min increments color coded from yellow to purple. A hydrophone location is presented by a red triangle on top of the ETOPO1 bed topography (2 km) map (NOAA National Geophysical Data Center, 2009) (b) Slope of *T*-wave envelopes versus origin time. Small events have relatively short-rising times leading to difficulties in fitting properly due to a short time window (e.g., a few scattered values estimated near 05:15). The temporal changes in slope may indicate vertical migration of swarms to deeper locations.

the elevation change of bathymetry in the region where abyssal T waves are emerged could not be negligible in many cases. In other words, the bathymetry effect can be dominant over that of seismic source in shaping T waves. However, we found that anisotropic source radiation and focal depth variation also make notable changes in the T-wave envelopes with the simplest seafloor geometry although it warrants further sophisticated numerical experiments with realistic bathymetry in the future.

Conclusion

We developed a 3D numerical model to synthesize abyssal T waves dealing with elastic-wave energy propagation in the heterogeneous oceanic crust for double-couple seismic sources and performed experiments for various fault types and source depths. The 3D modeling technique includes the effects of anisotropic source radiation and multiple scattering in the oceanic crust not properly applied by previous T-wave modeling studies. The modeling results show that (1) the total amount of radiated SV energy varies depending upon focal mechanisms, which causes a significant difference in the intensity of T waves; (2) anisotropic source radiation of a double-couple source causes directional changes in T waves; and (3) deeper earthquakes cause gentle-sloped envelopes, but fault type also affects the slopes.

The modeling results imply that determining the source depth, magnitude, and fault orientation from T waves using inversion methods is not a simple task. However, we can estimate the relative depths and source magnitudes from T waves for volcanic earthquake swarms or tectonic earthquake sequences that occur in similar volcanotectonic settings and with similar source mechanisms. When there is a "reference"

TABLE 2
Normalized Total Acoustic Energy Converted into Water Column on the Seafloor

Source Depth	Normal-Fault Event	Strike-Slip-Fault Event
5 km	1	0.36
10 km	0.87	0.33
15 km	0.75	0.30

event, where the earthquake source parameters can be defined by the land-seismic arrays, hydroacoustic modeling techniques presented here might provide insights into earthquake depth and magnitude information about the smaller magnitude earthquakes not detected by seismic arrays.

Although our synthetic envelopes successfully elucidated the influence of focal depth and mechanism on abyssal *T* waves, determining exact source information through hydroacoustic observation alone remains challenging. However, hydroacoustic observations are often the only way to investigate marine tectonic activities far from land-based seismic networks. We have found it is important to focus analyses on earthquake clusters from one volcanotectonic setting (i.e., repeated earthquakes along a given fault system, volcanic eruptions, and and/or hydrothermal vents) and by similar source mechanisms and propagation paths, which is required to properly use hydroacoustic techniques.

Data and Resources

Codes to construct synthetic *T* waves may be requested from the authors. The hydroacoustic observation data are available at Harvard dataverse. The accession numbers for our data sets at Harvard dataverse are available at DOI: 10.7910/DVN/RXCBX. The supplemental material for this article includes three figures: simulation results for other source depths (10 and 15 km) and an example of a swarm event.

Declaration of Competing Interests

The authors declare that the research was conducted in the absence of any commercial or financial relationships that could be construed as a potential conflict of interest.

Acknowledgments

This work was sponsored by a research grant from the Korean Ministry of Oceans and Fisheries (KIMST20190361; PM21020) and the National Oceanic and Atmospheric Administration (NOAA)/Pacific Marine Environmental Laboratory Contribution Number 5206. The authors thank two anonymous reviewers who helped them to greatly improve the original article. S. Y. and W. S. L. devised the project and wrote the text. S. Y. performed numerical simulations and W. S. L. prepared figures. W. S. L., R. P. D., and H. M. provided hydroacoustic data. All authors contributed to article edits.

References

Abercrombie, R. E., and G. Ekström (2001). Earthquake slip on oceanic transform faults, *Nature* **410,** 74–77.

Aki, K., and P. G. Richards (2002). *Quantitative Seismology*, Second Ed., University Science Books, New York, New York.

Balanche, A., C. Guennou, J. Goslin, and C. Mazoyer (2009). Generation of hydroacoustic signals by oceanic subseafloor earthquakes: A mechanical model, *Geophys. J. Int.* **177,** 476–480.

Bohnenstiehl, D. R., R. P. Dziak, H. Matsumoto, and T. K. A. Lau (2013). Underwater acoustic records from the March 2009 eruption of Hunga Ha'apai-Hunga Tonga volcano in the Kingdom of Tonga, *J. Volcanol. Geotherm. Res.* **249,** 12–24.

Bohnenstiehl, D. R., M. Tolstoy, D. K. Smith, C. G. Fox, and R. P. Dziak (2003). Time-clustering behavior of spreading-center seismicity between 15 and 35°N on the Mid-Atlantic Ridge: Observations from hydroacoustic monitoring, *Phys. Earth. Planet. In.* **138,** 147–161.

Boore, D. M., and J. Boatwright (1984). Average body-wave radiation coefficients, *Bull. Seismol. Soc. Am.* **74,** 1615–1621.

Brekhovskikh, L. M., and Yu. P. Lysanov (2003). *Fundamentals of Ocean Acoustics*, Third Ed., AIP Press/Springer-Verlag, New York, New York.

de Groot-Hedlin, C. D., and J. A. Orcutt (1999). Synthesis of earthquake-generated T-waves, *Geophys. Res. Lett.* **26,** 1227–1230.

de Groot-Hedlin, C. D., and J. A. Orcutt (2001). Excitation of *T*-phases by seafloor scattering, *J. Acoust. Soc. Am.* **109,** 1944–1954.

Dziak, R. P. (2001). Empirical relationship of *T*-wave energy and fault parameters of northeast Pacific Ocean earthquakes, *Geophys. Res. Lett.* **28,** 2537–2540.

Dziak, R. P., and C. G. Fox (1999). Long-term seismicity and ground deformation at Axial Volcano, Juan de Fuca Ridge, *Geophys. Res. Lett.* **26,** 3641–3644.

Dziak, R. P., C. G. Fox, H. Matsumoto, and A. E. Schreiner (1997). The April 1992 Cape Mendocino earthquake sequence: Seismo-acoustic analysis utilizing fixed hydrophone arrays, *Mar. Geophys. Res.* **19,** 137–162.

Dziak, R. P., C. G. Fox, and A. E. Schreiner (1995). The June-July 1993 seismo-acoustic event at CoAxial segment, Juan de Fuca Ridge: Evidence for a lateral dike injection, *Geophys. Res. Lett.* **22,** 135–138.

Dziak, R. P., M. Park, W. S. Lee, H. Matsumoto, D. R. Bohnenstiehl, and J. H. Haxel (2010). Tectonomagmatic activity and ice dynamics in the Bransfield Strait back-arc basin, Antarctica, *J. Geophys. Res.* **115,** no. B1, doi: 10.1029/2009JB006295.

Ergin, K. (1952). Energy ratio of the seismic waves reflected and refracted at a rock-water boundary*, *Bull. Seismol. Soc. Am.* **42,** 349–372.

Fox, C. G., H. Matsumoto, and T.-K. A. Lau (2001). Monitoring Pacific Ocean seismicity from an autonomous hydrophone array, *J. Geophys. Res.* **106,** 4183–4206.

Fukao, Y., E. Fujita, S. Hori, and K. Kanjo (1998). Response of a volcanic conduit to step-like change in magma pressure, *Geophys. Res. Lett.* **25,** 105–108.

Gusev, A. A. (1995). Vertical profile of turbidity and coda Q, *Geophys. J. Int.* **123,** 665–672.

Hoshiba, M. (1997). Seismic coda wave envelope in depth-dependent S wave velocity structure, *Phys. Earth. Planet. In.* **104,** 15–22.

Jamet, G., C. Guennou, L. Guillon, C. Mazoyer, and J. Y. Royer (2013). *T*-wave generation and propagation: A comparison between data and spectral element modeling, *J. Acoust. Soc. Am.* **134,** 3376–3385.

Johnson, R. H., and J. Northrop (1966). A comparison of earthquake magnitude with T-phase strength, *Bull. Seismol. Soc. Am.* **56,** 119–124.

Johnson, R. H., J. Northrop, and R. Eppley (1963). Sources of Pacific T phases. *J. Geophys. Res.* **68,** 4251–4260.

Kazahaya, K., H. Shinohara, and G. Saito (1994). Excessive degassing of Izu-Oshima volcano: Magma convection in a conduit, *Bull. Volcanol.* **56,** 207–216.

Lee, W. S., H. Sato, and K. Lee (2003). Estimation of *S*-wave scattering coefficient in the mantle from envelope characteristics before and after the *ScS* arrival, *Geophys. Res. Lett.* **30,** no. 24, doi: 10.1029/2003GL018413.

Lee, W. S., H. Sato, and K. Lee (2006). Scattering coefficients in the mantle revealed from the seismogram envelope analysis based on the multiple isotropic scattering model, *Earth Planet. Sci. Lett.* **241,** 888–900.

NOAA National Geophysical Data Center (2009). ETOPO1 1 Arc-Minute Global Relief Model, *NOAA National Centers for Environmental Information*, doi: 10.7289/V5C8276M.

Ogiso, M., H. Matsubayashi, and T. Yamamoto (2015). Descent of tremor source locations before the 2014 phreatic eruption of Ontake volcano, Japan, *Earth Planets Space* **67,** doi: 10.1186/s40623-015-0376-y.

Okal, E. A., and J. Talandier (1986). *T*-wave duration, magnitudes and seismic moment of an earthquake-application to tsunami warning, *J. Phys. Earth.* **34,** 19–42.

Okal, E. A., P. Alasset, O. Hyvernaud, and F. Schindelé (2003). The deficient T waves of tsunami earthquakes, *Geophys. J. Int.* **152,** 416–432.

Pan, J., and A. M. Dziewonski (2005). Comparison of mid-oceanic earthquake epicentral differences of travel time, centroid locations, and those determined by autonomous underwater hydrophone arrays, *J. Geophys. Res.* **110,** no. B7, doi: 1029/2003JB002785.

Park, M., R. I. Odom, and D. J. Soukup (2001). Modal scattering: A key to understanding oceanic *T*-waves, *Geophys. Res. Lett.* **28,** 3401–3404.

Sato, H., and M. C. Fehler (1998). *Seismic Wave Propagation and Scattering in the Heterogeneous Earth*, AIP Press/Springer-Verlag, New York, New York.

Schreiner, A. E., C. G. Fox, and R. P. Dziak (1995). Spectra and magnitudes of *T*-waves from the 1993 earthquake swarm on the Juan de Fuca Ridge, *Geophys. Res. Lett.* **22,** 139–142.

Shearer, P. M. (1999). *Introduction to Seismology*, Cambridge University Press, Cambridge, New York, New York.

Swift, S. A., D. Lizarralde, R. A. Stephen, and H. Hoskins (1998). Velocity structure in upper ocean crust at Hole 504B from vertical seismic profiles, *J. Geophys. Res.* **103,** 15,361–15,376.

Talandier, J., and E. A. Okal (1998). On the mechanism of conversion of seismic waves to and from T waves in the vicinity of island shores, *Bull. Seismol. Soc. Am.* **88,** 621–632.

Tolstoy, I., and M. Ewing (1950). The T phase of shallow-focus earthquakes, *Bull. Seismol. Soc. Am.* **40,** 25–51.

Tolstoy, M., J. P. Cowen, E. T. Baker, D. J. Fornari, K. H. Rubin, T. M. Shank, F. Waldhauser, D. R. Bohnenstiehl, D. W. Forsyth, R. C. Holmes, *et al.* (2006). A sea-floor spreading event captured by seismometers, *Science* **314,** 1920–1922.

Venkataraman, A., and H. Kanamori (2004). Effect of directivity on estimates of radiated seismic energy, *J. Geophys. Res.* **109,** no. B4, doi: 10.1029/2003JB002548.

Walker, D. A., C. S. McCreery, and Y. Hiyoshi (1992). T-phase spectra, seismic moments, and tsunamigenesis, *Bull. Seismol. Soc. Am.* **82,** 1275–1305.

Yang, Y., and D. W. Forsyth (2003). Improving epicentral and magnitude estimation of earthquakes from T Phases by considering the excitation function, *Bull. Seismol. Soc. Am.* **93,** 2106–2122.

Yoshimoto, K. (2000). Monte Carlo simulation of seismogram envelopes in scattering media, *J. Geophys. Res.* **105,** 6153–6161.

Manuscript received 19 September 2021
Published online 19 April 2022